Research Article

Dongyang Yan, Ran Mei, Mingyan Li, Zhikai Ma, Zhi Hong Hang* and Jie Luo*

Controlling coherent perfect absorption via long-range connectivity of defects in three-dimensional zero-index media

https://doi.org/10.1515/nanoph-2023-0485
Received July 31, 2023; accepted October 13, 2023;
published online October 25, 2023

Abstract: Coherent perfect absorption (CPA), as time-reversed lasing, arises from appropriate wave interference within absorbers, offering flexible control over wave absorption. Typically, this control involves tuning the phase difference between two counter-propagating incident beams. Here, we elucidate the critical role of defect connectivity within three-dimensional zero-index media for realizing and controlling CPA. Specifically, the realization of CPA critically depends on the establishment of long-range connectivity of defects in a specific direction. Once the long-range connectivity is established, the CPA exhibits remarkable resilience against defects' deformation, changes in size and shape of the zero-index media, as well as variations in number and orientation of incident channels. Notably, a minor disruption to this connectivity will result in a complete reduction of absorption to zero, highlighting an ultra-sensitive absorption property in response to connectivity perturbations. Our findings not only unveil a physical mechanism for realizing CPA but also open up promising avenues for advanced CPA control with versatile functionalities.

***Corresponding authors: Zhi Hong Hang**, School of Physical Science and Technology and Collaborative Innovation Center of Suzhou Nano Science and Technology, Soochow University, Suzhou 215006, China; Institute for Advanced Study, Soochow University, Suzhou 215006, China; and Provincial Key Lab of Thin Films, Soochow University, Suzhou 215006, China, E-mail: zhhang@suda.edu.cn; and **Jie Luo**, Institute of Theoretical and Applied Physics, School of Physical Science and Technology, Soochow University, Suzhou 215006, China; and Provincial Key Lab of Thin Films, Soochow University, Suzhou 215006, China, E-mail: luojie@suda.edu.cn. https://orcid.org/0000-0002-3614-3375 (J. Luo)

Dongyang Yan, **Ran Mei and Mingyan Li**, Institute of Theoretical and Applied Physics, School of Physical Science and Technology, Soochow University, Suzhou 215006, China

Zhikai Ma, State Key Laboratory for Mesoscopic Physics and Frontiers Science Center for Nano-optoelectronics, School of Physics, Peking University, Beijing 100871, China

Keywords: coherent perfect absorption; zero-index media; long-range connectivity; absorption control; geometry-invariance

1 Introduction

Perfect absorption of electromagnetic waves is of great interest and importance across diverse applications including photovoltaics and stealth technologies [1–3]. In the past decade, a unique way to achieve perfect absorption with more than one incident beam, i.e., coherent perfect absorption (CPA) [4–7], has witnessed rapid advancements. Conceptually resembling time-reversed lasers, CPA arises from appropriate wave interference within absorbers. Notably, the CPA scheme surpasses traditional absorption configurations by providing flexible control over wave absorption, allowing continuous adjustment from 100 % to zero absorption through phase difference tuning among incident beams, without modulating intrinsic nonlinearity and absorption coefficient [4–7]. This makes CPA particularly attractive to applications of modulators, switches, and transducers. Up to now, diverse types of CPA implementations have emerged, including the CPA-lasing [8–14], broadband CPA [15–21], and geometry-invariant CPA [22, 23], etc. The geometry-invariant CPA based on zero-index media (ZIM) [24–32] is of special interest. Unlike standard CPA scenarios, where perfect absorption occurs under the illumination of two counter-propagating beams, geometry-invariant CPA allows for more than two incident beams, thereby offering additional degrees of freedom to manipulate wave absorption. However, the previously proposed geometry-invariant CPA schemes primarily rely on two-dimensional (2D) photonic-doped ZIM, which may constrain their practical applications in three-dimensional (3D) space. In addition, the additional dimension-introduced new physics to realize the CPA and extra degrees of freedoms to tune the absorption in 3D models are worth exploring.

Nevertheless, the principle of the geometry-invariant CPA in 2D ZIM is inapplicable to 3D systems due to

fundamental differences in electromagnetic wave behaviors. In 2D ZIM, electromagnetic waves follow scalar wave equations, while in 3D ZIM, they obey vector wave equations. Consequently, numerous electromagnetic properties of 2D and 3D ZIM exhibit fundamental distinctions [13, 33–36]. For instance, the photonic doping effect [37–42], which serves as the basis for geometry-invariant CPA in 2D ZIM, is absent in 3D ZIM. Instead, unusual phenomena like electromagnetic wave percolation [33] and photonic antidoping effect [13, 34] are observed in 3D ZIM when embedded with defects. However, these phenomena cannot be exploited to achieve CPA, as the embedded defects do not affect the absorption at all. Therefore, novel physical mechanisms must be explored to realize the geometry-invariant CPA based on 3D ZIM.

In this work, we elucidate the critical role of defect connectivity within 3D ZIM for achieving and controlling the CPA. We demonstrate that the successful realization of CPA crucially relies on the establishment of long-range connectivity of defects in a specific direction. Once this long-range connectivity is established, geometry-invariant multichannel CPA can be obtained, which exhibits remarkable resilience against defects' deformation, changes in size and shape of the ZIM, as well as variations in number and orientation of incident channels (Figure 1(a)). Interestingly, even a minor disruption, such as a small gap, will break the long-range connectivity and result in a complete reduction of absorption to zero (Figure 1(b)), highlighting an ultra-sensitive absorption property in response to connectivity perturbations. To practically demonstrate these exceptional properties, a practical design using photonic crystals (PhCs) embedded with conductive films is demonstrated. Our work not only unveils a physical mechanism underlying the realization and control of CPA in 3D ZIM but also opens up possibilities for developing ultra-sensitive sensors.

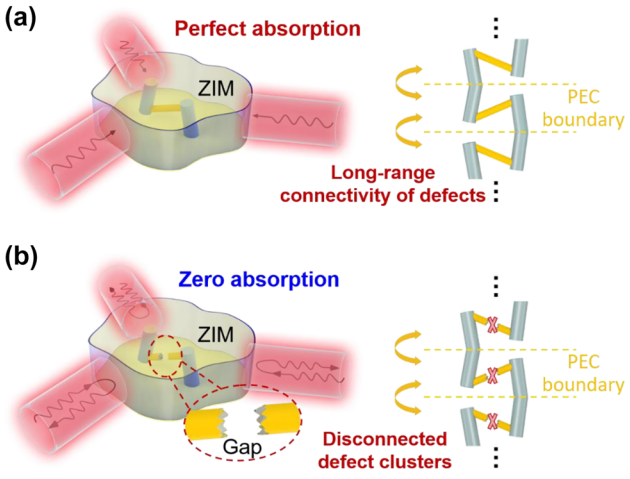

Figure 1: Schematic graphs of geometry-invariant three-channel CPA based on a 3D ZIM embedded with absorptive defects. Such CPA is critically sensitive to the establishment of long-range connectivity of defects in the vertical direction. (a) The defect cluster forms a continuous connection between the upper and lower PEC plates. Since PEC boundaries can be viewed as mirror symmetry planes, the long-range connectivity of defects in the vertical direction is established, in which case CPA is obtained. (b) A minor disruption, such as a small gap, in the defect connectivity will break the long-range connection, and mirrored defects will form separated clusters that are disconnected with each other in the vertical direction. In this case, there is no absorption.

2 Results

2.1 Connectivity-controlled CPA and the underlying physics

To explore the physical mechanisms underlying the realization and control of CPA based on 3D ZIM, we adopt a two-channel model for simplicity, as schematically shown in Figure 2(a). The model comprises a 3D ZIM slab (relative permittivity $\varepsilon_{\mathrm{ZIM}} \sim 0$, relative permeability $\mu_{\mathrm{ZIM}} \sim 0$, $l_x \times l_y \times l_z$ in dimension) embedded with two thick dielectric cylindrical defects (radius r_1, length l_1, relative permittivity ε_1), interconnected by a thin perfect electric conductor (PEC) cylindrical defect (radius r_2, length l_2). This ZIM slab is placed inside a PEC – perfect magnetic conductor (PMC) waveguide (cross section $l_x \times l_z$ in dimension), which supports transverse electromagnetic waves without cutoff frequencies [43].

We consider two counter-propagating planer waves with electric fields polarized along the z direction, incident normally onto the ZIM slab from free space (Figure 2(a)). The two incident waves are in phase with identical amplitude. Their electric and magnetic fields for left (or right) incidence can be expressed as follows: $\mathbf{E}_{\mathrm{in}}^{\mathrm{L}} = \hat{\mathbf{z}} E_0 \mathrm{e}^{-i\omega t + ik_0 y}$ and $\mathbf{H}_{\mathrm{in}}^{\mathrm{L}} = \hat{\mathbf{x}} E_0 / Z_0 \mathrm{e}^{-i\omega t + ik_0 y}$ (or $\mathbf{E}_{\mathrm{in}}^{\mathrm{R}} = \hat{\mathbf{z}} E_0 \mathrm{e}^{-i\omega t - ik_0 (y - l_y)}$ and $\mathbf{H}_{\mathrm{in}}^{\mathrm{R}} = -\hat{\mathbf{x}} E_0 / Z_0 \mathrm{e}^{-i\omega t - ik_0 (y - l_y)}$), where E_0, ω, k_0, and Z_0 are the electric field amplitude, angular frequency, wave number in free space, and characteristic impedance of free space, respectively. Due to the infinitely long wavelength within the ZIM arising from $\varepsilon_{\mathrm{ZIM}} \sim 0$ and $\mu_{\mathrm{ZIM}} \sim 0$, only transverse electromagnetic waves are supported in the ZIM region. Consequently, despite the presence of cylindrical defects, the electric and magnetic fields on the left and right xz surfaces of the ZIM slab remain nearly uniform. Under this circumstance, we can express the electric and magnetic fields of the backward propagating waves in the left region as follows: $\mathbf{E}_{\mathrm{back}}^{\mathrm{L}} = \hat{\mathbf{z}} R_L E_0 \mathrm{e}^{-i\omega t - ik_0 y}$ and $\mathbf{H}_{\mathrm{back}}^{\mathrm{L}} = -\hat{\mathbf{x}} R_L E_0 / Z_0 \mathrm{e}^{-i\omega t - ik_0 y}$. These fields are the superposition of

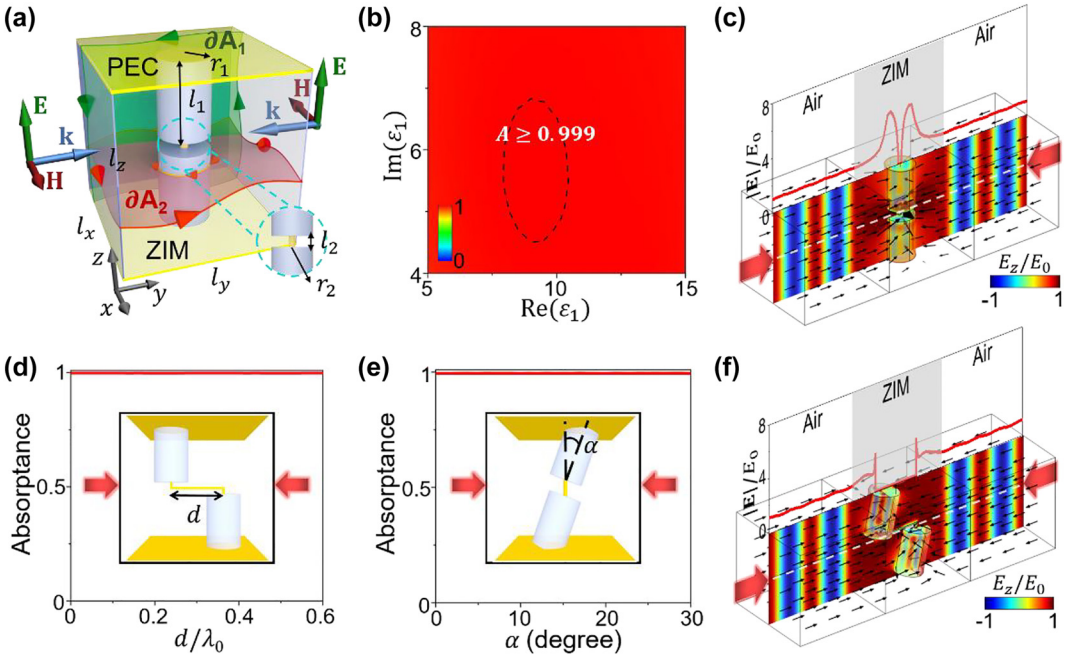

Figure 2: Realization of robust CPA in the presence of long-range connectivity of defects. (a) Schematic graph of a two-channel CPA model consisting of a 3D ZIM slab inside a PEC-PMC waveguide. Inside the ZIM slab, two thick cylindrical defects connecting the upper and lower PEC plates are interconnected by a thin PEC cylindrical defect. Curves ∂A_1 (green) and ∂A_2 (red) represent the boundaries of vertical and horizontal integral surfaces, respectively. Two counter-propagating planer waves with electric fields polarized along the z direction are normally incident onto the ZIM slab from free space. (b) Absorptance with respect to $\mathrm{Re}(\varepsilon_1)$ and $\mathrm{Im}(\varepsilon_1)$ of the thick cylinders. (c) Simulated E_z/E_0 (color), time-averaged energy flux (arrows), and $|\mathbf{E}|/E_0$ (red line) along the white dashed line for the model in (a) with $\varepsilon_1 = 9 + 5.5i$. (d) Absorptance variation when there is a lateral shift of d along the y direction between the two thick cylinders. (e) Absorptance variation when the cylinder cluster is rotated by an angle of α measured from the z axis. In (d) and (e), the upper and lower thick cylinders are always interconnected by the thin PEC cylinder, as illustrated by the insets. (f) Simulated E_z/E_0 (color), time-averaged energy flux (arrows), and $|\mathbf{E}|/E_0$ (red line) along the white dashed line when changing both the position and orientation of the cylinder cluster.

the reflected waves from the left incidence and the transmitted waves from the right incidence. Similarly, the electric and magnetic fields of the forward propagating waves in the right region are given by $\mathbf{E}^{\mathrm{R}}_{\mathrm{back}} = \hat{\boldsymbol{z}} R_R E_0 \mathrm{e}^{-i\omega t + ik_0(y-l_y)}$ and $\mathbf{H}^{\mathrm{R}}_{\mathrm{back}} = \hat{\boldsymbol{x}} R_R E_0/Z_0 \mathrm{e}^{-i\omega t + ik_0(y-l_y)}$, respectively. Here, R_L and R_R are two unknown coefficients to be determined.

Next, we apply the Maxwell's equations, i.e., $\oint_{\partial A_1} \mathbf{E}\cdot\mathrm{d}\mathbf{l} = i\omega\mu_{\mathrm{ZIM}} \iint_{A_1} \mathbf{H}\cdot\mathrm{d}\mathbf{S}$ and $\oint_{\partial A_2} \mathbf{H}\cdot\mathrm{d}\mathbf{l} = -i\omega\varepsilon_{\mathrm{ZIM}} \iint_{A_2} \mathbf{E}\cdot\mathrm{d}\mathbf{S}$ to the ZIM. Here, ∂A_1 and ∂A_2 represent the boundaries of the vertical integral surface A_1 and horizontal integral surface A_2, as indicated by green and red lines in Figure 2(a), respectively. Due to the properties of $\varepsilon_{\mathrm{ZIM}} \sim 0$ and $\mu_{\mathrm{ZIM}} \sim 0$, the two equations simplify to:

$$\oint_{\partial A_1} \mathbf{E}\cdot\mathrm{d}\mathbf{l} = 0, \tag{1a}$$

and

$$\oint_{\partial A_2} \mathbf{H}\cdot\mathrm{d}\mathbf{l} = 0. \tag{1b}$$

The integral $\oint_{\partial A_1} \mathbf{E}\cdot\mathrm{d}\mathbf{l}$ (or $\oint_{\partial A_2} \mathbf{H}\cdot\mathrm{d}\mathbf{l}$) generally comprises two components: an integral around the ZIM denoted as $\oint_{\partial A_{1,Z}} \mathbf{E}\cdot\mathrm{d}\mathbf{l}$ (or $\oint_{\partial A_{2,Z}} \mathbf{H}\cdot\mathrm{d}\mathbf{l}$) and an integral around the embedded defects represented as $\oint_{\partial A_{1,D}} \mathbf{E}\cdot\mathrm{d}\mathbf{l}$ (or $\oint_{\partial A_{2,D}} \mathbf{H}\cdot\mathrm{d}\mathbf{l}$). Considering the fact that the tangential electric (or magnetic) fields on the PEC (or PMC) boundaries are zero, we obtain $\oint_{\partial A_{1,Z}} \mathbf{E}\cdot\mathrm{d}\mathbf{l} = (R_R - R_L)E_0 l_z \mathrm{e}^{-i\omega t}$ and $\oint_{\partial A_{2,Z}} \mathbf{H}\cdot\mathrm{d}\mathbf{l} = (2 - R_R - R_L)E_0 l_x/Z_0 \mathrm{e}^{-i\omega t}$. Consequently, Eq. (1) can be reformulated as follows:

$$\oint_{\partial A_{1,D}} \mathbf{E}\cdot\mathrm{d}\mathbf{l} = (R_L - R_R)E_0 l_z \mathrm{e}^{-i\omega t}, \tag{2a}$$

and

$$\oint_{\partial A_{2,D}} \mathbf{H}\cdot\mathrm{d}\mathbf{l} = (R_R + R_L - 2)E_0 l_x/Z_0 \mathrm{e}^{-i\omega t}. \tag{2b}$$

The CPA requires that $R_R = R_L = 0$. In this case, Eq. (2) is simplified to,

$$\oint_{\partial A_{1,D}} \mathbf{E}\cdot\mathrm{d}\mathbf{l} = 0, \tag{3a}$$

and

$$\oint_{\partial A_2, D} \mathbf{H} \cdot \mathrm{d}\mathbf{l} = -2E_0 l_x / Z_0 \mathrm{e}^{-i\omega t}. \tag{3b}$$

Equation (3) presents the essential condition for CPA, which holds for any kind of defects and integral surfaces. If there exists an integral surface A_1 that does not intersect with any defects' domain, or in other words, the entire surface A_1 is embedded within the ZIM, then Eq. (3a) will be satisfied. Conversely, any selected integral surface A_2 must intersect with the defects' domain; otherwise, Eq. (3b) cannot be fulfilled. These conditions on integral surfaces impose requirements on the defect connectivity inside the ZIM, that is, the defects must exhibit the long-range connectivity in the z direction, while generally remaining disconnected in the x direction to achieve CPA.

To fulfill the requirements on defect connectivity, the cylinder cluster depicted in Figure 2(a) establishes a continuous connection between the upper and lower PEC plates. Since the PEC plates can be viewed as mirror symmetry planes, they create mirror images of the connected cylinders. As a result, the long-range connectivity of cylinders is established along the z direction. This configuration ensures the necessary connectivity conditions for CPA realization.

To endow the ZIM slab with absorption capability, we assume the two thick dielectric cylinders to be dissipative, characterized by a complex relative permittivity ε_1. In order to identify the parameter combinations leading to maximal absorption, we plot the absorptance as a function of the real part of ε_1 (i.e., $\mathrm{Re}(\varepsilon_1)$) and imaginary part of ε_1 (i.e., $\mathrm{Im}(\varepsilon_1)$), as presented in Figure 2(b). The relevant parameters are set as $l_x = l_y = l_z = 2\lambda_0, r_1 = 0.3\lambda_0, l_1 = 0.9\lambda_0, r_2 = 0.03\lambda_0$, and $l_2 = 0.2\lambda_0$, where λ_0 is the free-space wavelength, fixed in the numerical calculations. The methods for absorptance computation are presented in Supporting Information. We see that the absorption reaches near-100 % when $\varepsilon_1 = 9 + 5.5i$, indicating successful realization of CPA. Importantly, the absorption remains significantly high as variations of ε_1, signifying the robustness of the CPA. To validate the CPA behavior, we conduct numerical simulations using the finite-element software COMSOL Multiphysics. Figure 2(c) displays the simulated E_z/E_0 (color), time-averaged energy flux (arrows), and $|\mathbf{E}|/E_0$ (red line) along the white dashed line for the model with $\varepsilon_1 = 9 + 5.5i$ under the illumination of two counter-propagating planer waves. The E_z/E_0 profile shows the wave behavior in the whole model, in which strong electric field is observed inside the absorptive dielectric cylinders. On the other hand, from the $|\mathbf{E}|/E_0$ profile, constant electric field amplitude is observed in the air regions, indicating the disappearance of standing waves due to the interference of incident and reflected waves. Thus, we obtain near-zero reflection and almost perfect on the ZIM slab. In fact, both the incident waves are fully absorbed by the two thick dissipative cylinders, as evidenced by the energy flux distributions. These results conclusively demonstrate the occurrence of CPA in the 3D ZIM system.

It is noteworthy that the CPA is remarkably robust against the deformation of the embedded cylinders, as long as the long-range connectivity along the z direction is maintained. To demonstrate this robustness, we consider a lateral shift d in the y direction between the upper and lower thick cylinders, as well as a rotation angle α of the cylinder cluster measured from the z axis, as illustrated by the insets in Figure 2(d) and (e). The absorptance for both cases is presented in Figure 2(d) and (e), respectively, revealing robust near-perfect absorption. We further verify the robustness by simulating the E_z/E_0 (color), time-averaged energy flux (arrows), and $|\mathbf{E}|/E_0$ (red line) along the white dashed line when changing both the position and orientation of the cylinder cluster (Figure 2(f)). Notably, near-constant electric field amplitude is observed in the air regions, confirming the robustness of CPA based on 3D ZIM against the deformation of the embedded cylinders in the presence of long-range connectivity.

However, it is crucial to note that a minor disruption to this long-range connectivity will lead to a complete reduction of absorption, resulting in 100 % reflection and zero absorption of incident waves. Once the long-range connectivity along the z direction is broken for the model in Figure 2(a), we can always find out integral surfaces A_1 and A_2 that do not intersect with any cylinder. Hence, we have

$$\oint_{\partial A_1, D} \mathbf{E} \cdot \mathrm{d}\mathbf{l} = 0, \tag{4a}$$

and

$$\oint_{\partial A_2, D} \mathbf{H} \cdot \mathrm{d}\mathbf{l} = 0. \tag{4b}$$

Combining with Eq. (2), we obtain $R_L = R_R = 1$, indicating zero absorption in this case. As an example for verification, we cut the thin PEC cylinder to create a gap of $0.1\lambda_0$ (Figure 3(a)). The absorptance map displayed in Figure 3(b) shows completely zero absorption as the variations of ε_1. This implies that the CPA is impossible in this scenario. In addition, we re-simulate the model in Figure 2(c), but with a gap of $0.1\lambda_0$ in the central thin PEC cylinder. From the simulation results, standing waves with normalized amplitudes oscillating from 0 to 2 in the air regions ($|\mathbf{E}|/E_0$ profile) and zero electric field inside the thick cylinders (E_z/E_0 profile) are observed, indicating 100 % reflection and zero absorption of incident waves, as further evidenced by the zero electric field within the thick cylinders.

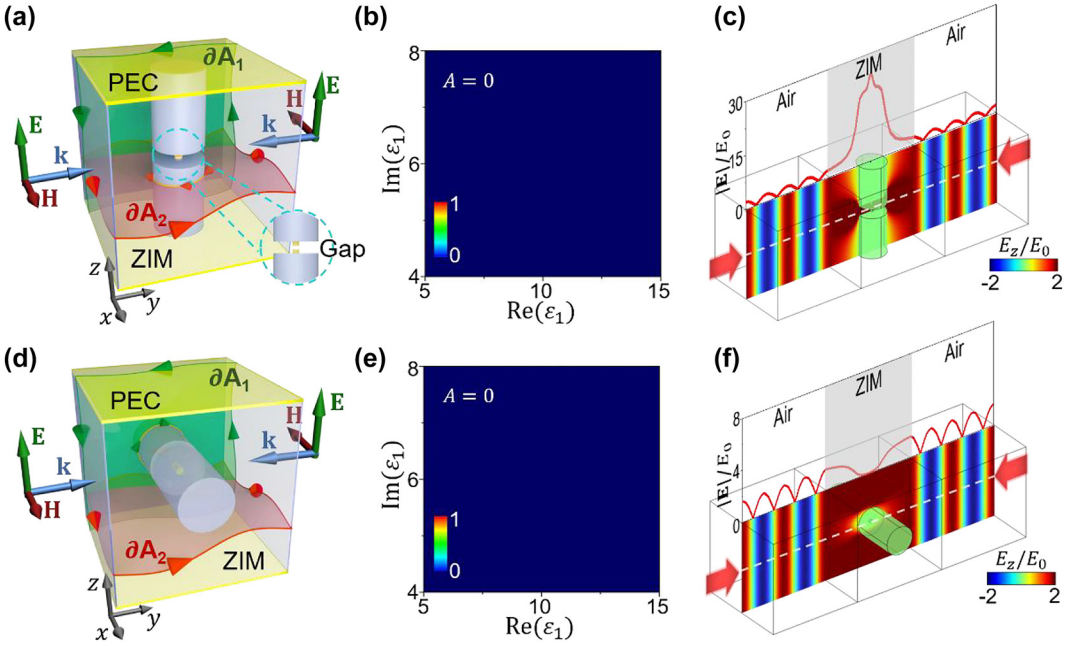

Figure 3: Zero absorption in the absence of long-range connectivity of defects in the vertical direction. (a) Schematic graph of the two-channel CPA model when the central thin PEC cylinder is cut to create a gap of $0.1\lambda_0$. (b) Absorptance with respect to $\mathrm{Re}(\varepsilon_r)$ and $\mathrm{Im}(\varepsilon_r)$ of the thick cylinders for the model in (a). (c) Simulated E_z/E_0 (color) and $|\mathbf{E}|/E_0$ (red line) along the white dashed line for the model in (a) with $\varepsilon_r = 9 + 5.5i$. (d) Schematic graph of the two-channel CPA model when the cylinder cluster is rotated to be oriented along the x direction. (e) Absorptance with respect to $\mathrm{Re}(\varepsilon_r)$ and $\mathrm{Im}(\varepsilon_r)$ of the thick cylinders for the model in (d). (f) Simulated E_z/E_0 (color) and $|\mathbf{E}|/E_0$ (red line) along the white dashed line for the model in (d) with $\varepsilon_r = 9 + 5.5i$.

In the second example, we rotate the cylinder cluster to be oriented along the x direction (Figure 3(d)). In this case, we have $\oint_{\partial A_2, D}\mathbf{H}\cdot\mathrm{d}\mathbf{l} = 0$. According to Eq. (2b), we obtain $R_R + R_L = 2$. This indicates that $R_L = R_R = 1$, also implying 100 % reflection of incident waves. As expected, zero absorption, irrespective of ε_1, is observed in the absorptance map in Figure 3(e). This zero absorption property is further verified by the presence of standing waves in the air regions and zero electric fields inside the thick cylinders (Figure 3(f)). The above results demonstrate that the CPA based on 3D ZIM is crucially sensitive to the connectivity perturbations, which provides an ultra-sensitive approach for controlling CPA.

It is noteworthy that although above connectivity-sensitive CPA is demonstrated for transverse-electromagnetic (TEM) modes inside the PEC-PMC waveguide, the principle is also applicable for transverse-electric (TE) and transverse-magnetic (TM) modes. A TE or TM mode can be viewed as the superposition of two TEM modes propagating at the same oblique angle [16]. Through designing the ZIM slab with appropriately inclined surfaces, the connectivity-controlled CPA can also be realized for TE and TM waves (see Supporting Information).

2.2 Connectivity-controlled geometry-invariant multichannel CPA

Superior to the traditional CPA of the two-channel configuration [4–6], the CPA based on 3D ZIM possesses a unique property of geometry-invariance and allows more than two input channels, offering additional degrees of freedom to control absorption. As a demonstration, we introduce a three-channel CPA model comprising an irregular 3D ZIM and a curved conductive film embedded within it (Figure 4(a)). The conductive film is designed to be ultrathin, with a thickness t much smaller than the waveguide λ_0. This ultrathin film can be characterized by a sheet resistance R_s, defined as $1/(\sigma_0 t)$ with σ_0 being the conductivity, measuring the in-plane resistance for a film of arbitrarily sized square shape [44]. Alternatively, it can be approximately characterized by a relative permittivity of $iZ_0/(k_0 t R_s)$ [44]. In practice, such a conductive film can be easily realized by a sheet of conductive materials like graphene and indium tin oxide at low frequencies [16, 19, 45]. The ZIM is positioned inside a PEC-PMC waveguide, consisting of upper and lower PEC plates and surrounding PMC plates. The embedded conductive film serves as a connecting link between the upper and lower PEC plates, establishing the long-range connectivity in

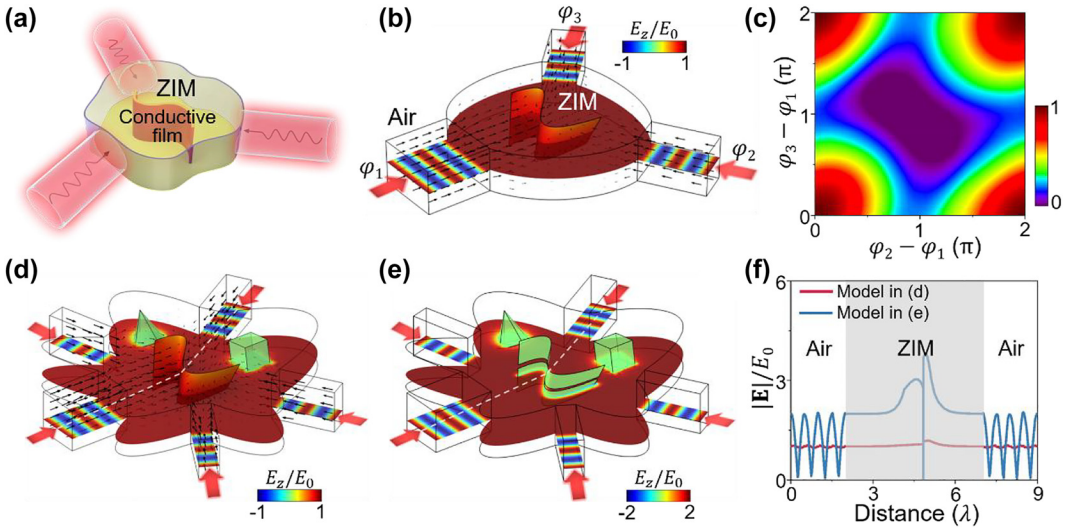

Figure 4: Connectivity-controlled geometry-invariant multichannel CPA. (a) Schematic graph of a three-channel CPA model consisting of an irregular 3D ZIM embedded with a curved conductive film. (b) Simulated E_z/E_0 (color) and time-averaged energy flux (arrows) for the three-channel model with $R_s = 0.9Z_0$. (c) Absorptance as a function of the phase differences among the three channels in (b). [(d) and (e)] Simulated E_z/E_0 (color) and time-averaged energy flux (arrows) in a five-channel model when additional two defects are embedded inside the ZIM. The curved conductive film connects upper and lower PEC plates in (d), but is cut to create a gap of $0.1\lambda_0$ in (e). (f) Simulated $|\mathbf{E}|/E_0$ along the white dashed lines in the models in (d) and (e).

the vertical direction. This configuration ensures the essential connectivity conditions for realizing CPA.

Figure 4(b) presents the simulation results for the three-channel model. In this configuration, three incident waves having the same phase and amplitude (with electric field polarized in the vertical direction) simultaneously impinge upon the ZIM from different directions. From the distributions of E_z/E_0 (color) and time-averaged energy flux (arrows), it is evident that all incident waves are absorbed by the embedded conductive film. Here, we set the sheet resistance of the conductive film as $R_s = 0.9Z_0$. Actually, even when the R_s deviates from this value, near-perfect absorption can still be obtained. Then, to investigate the tuning capability of the three-channel model, we modify the phases of the three incident waves, denoted as φ_1, φ_2, and φ_3, respectively. In Figure 4(c), we display the absorptance map as a function of the phase differences $\varphi_2 - \varphi_1$ and $\varphi_3 - \varphi_1$. It is seen that the perfect absorption occurs at a phase difference of 0 or 2π, and zero absorption occurs at a phase difference of π. By changing the phase difference either $\varphi_2 - \varphi_1$ or $\varphi_3 - \varphi_1$, the absorption can be tuned efficiently in an oscillatory manner.

Furthermore, introducing additional input channels allows for more degrees of freedom in controlling the absorption. We find that when dividing the three channels into more channels, while maintaining the total width of all channels unchanged, the required R_s remains unaffected. In Figure 4(d), we divide the three channels in Figure 4(b) into five channels while maintaining the total width unchanged. Additionally, two more defects are embedded within the ZIM, but these defects remain disconnected from the upper and lower PEC plates. These additional defects do not alter the connectivity characteristics of defects in this model. Furthermore, the size and shape of the ZIM are modified. Interestingly, we find that these changes do not affect the CPA behavior. The conductive film in Figure 4(d) is the same as that in Figure 4(b), and near-perfect absorption is achieved, as verified by the simulation results in Figure 4(d)–(f). These results demonstrate the realization of geometry-invariant multichannel CPA based on 3D ZIM, and highlight the robustness of CPA as long as the connectivity characteristics remain unchanged. However, it is important to note that if the long-range connectivity is disrupted, the absorption will immediately reduce to zero. As seen in Figure 4(e) and (f), when the conductive film is cut to create a gap of $0.1\lambda_0$, evident standing waves in the air regions are observed, indicating 100 % reflection and zero absorption of incident waves.

The above results demonstrate the intriguing properties of CPA based on 3D ZIM. Specifically, the CPA is highly robust against deformations of the embedded defects, changes in size and shape of the ZIM, as well as variations in number and orientation of incident channels, as long as the long-range connectivity is established. However, it is crucially sensitive to the perturbations to connectivity characteristics of defects. This connectivity-sensitive

geometry-invariant multichannel CPA offers promising possibilities for advanced and flexible control of wave absorption.

2.3 Practical implementation based on 3D PhCs

In the following, we will demonstrate a practical implementation of the connectivity-controlled CPA based on 3D ZIM. The key to the successful design lies in achieving 3D ZIM with low loss. Fortunately, 3D PhCs exhibiting Dirac-like cone dispersion offers a platform for realizing the low-loss 3D ZIM [31, 34, 46].

Here, we make use of a PhC composed of a simple cubic lattice of core–shell spheres with a lattice constant of a (Figure 5(a)). The core of the sphere is made of PEC (radius $r_c = 0.126a$), and the shell is made of a dielectric material (radius $r_s = 0.4a$, relative permittivity $\varepsilon_s = 30$). We note that this high-index dielectric material can be realized in the microwave regime [47]. In Figure 5(b), the left panel graph shows a Dirac-like cone at the center of the Brillouin zone (i.e., the Γ point) as the consequence of sixfold degenerate modes occurring at the normalized frequency of $\omega a/2\pi c = 0.2678$. Previous researches have demonstrated that at the Dirac-point frequency, the PhC effectively works as a uniform ZIM possessing vanishing permittivity and permeability simultaneously [31, 34, 46, 48–50]. The right panel graph shows the effective relative permittivity ε_{eff} and relative permeability μ_{eff} of this PhC, both of which are found to be zero at the Dirac-point frequency. Here, the effective parameters are retrieved based on the averaged eigen-fields [34, 51].

By utilizing this 3D PhC-based ZIM, we construct a two-channel CPA model comprising $3 \times 3 \times 4$ PhC units, strategically arranged as depicted in Figure 5(a). Within the PhC, an ultrathin conductive film strip (thickness $0.02a$, width a, sheet resistance $0.2Z_0$) connects the upper and lower surfaces, thus establishing the long-range connectivity in the vertical direction. Figure 5(c) presents the simulated E_z/E_0 (color) and $|\mathbf{E}|/E_0$ (red line) along the white dashed line under the illumination of two counter-propagating waves at the Dirac-point frequency. The nearly constant electric field amplitude observed in the air regions indicates the near-perfect absorption of incident waves. We find that the absorptance reaches an impressive value of 0.99 (Figure 5(e)). Next, we introduce a gap of a by cutting the conductive film. From the simulation results in Figure 5(d), a substantial amount of reflection is observed, leading to a significant reduction in absorptance to 0.09 (Figure 5(e)). This clearly shows the connectivity-controlled absorption behavior. For comparison, we remove the PhC, as shown in Figure 5(d) and (e). It is seen that the CPA disappears, and the sensitivity on the connectivity perturbations is diminished. In Supporting Information, the connectivity-controlled CPA is further demonstrated based on an alternative design, i.e., all-dielectric PhCs, which could be realized at higher

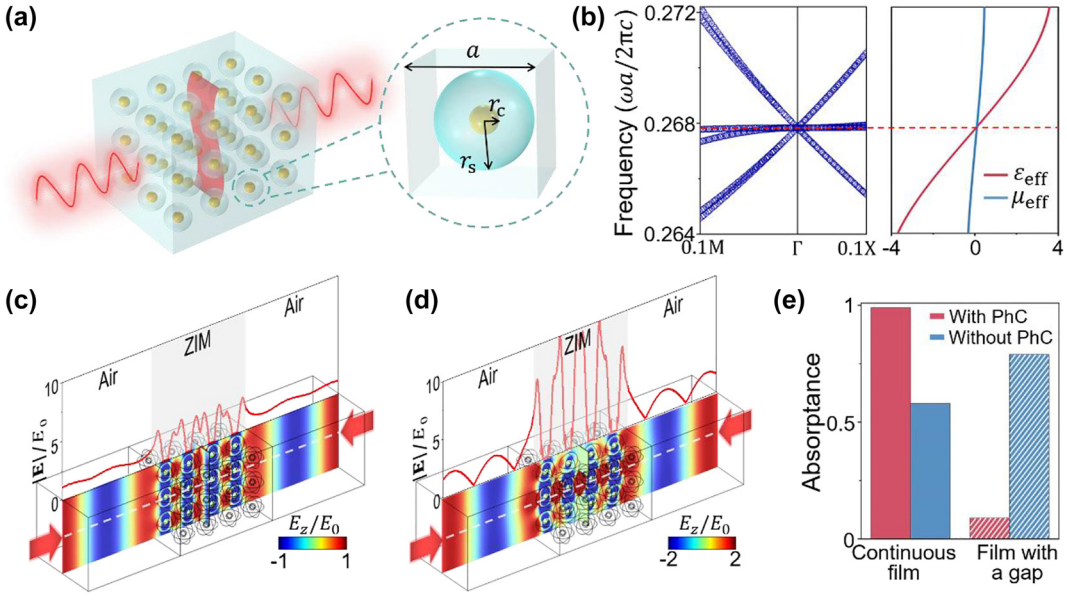

Figure 5: Practical implementation based on 3D PhCs. (a) A practical implementation a two-channel CPA using a 3D PhC-based ZIM. The PhC is composed of a simple cubic lattice of core–shell spheres. (b) Band structure of the PhC and its effective parameters ε_{eff} and μ_{eff} nearby the Dirac-point frequency. [(c) and (d)] Simulated E_z/E_0 (color) and $|\mathbf{E}|/E_0$ (red line) along the white dashed line under illumination of two counter-propagating waves. In (c), a strip of conductive film connecting the upper and lower boundaries is placed inside the PhC. In (d) the conductive film is cut to create a gap of a. (e) Absorptance for the models in (c) and (d) in the presence or absence of the PhC.

frequencies. Overall, the proposed implementation using 3D PhC-based ZIM has shown the feasibility and effectiveness in realizing and controlling CPA through engineering the defect connectivity.

3 Discussion and conclusion

Compared to the traditional CPA of the two-channel configuration [4–6], the implementation of CPA based on 3D ZIM offers the advantage of accommodating more than two input channels. This feature provides additional degrees of freedom to efficiently control absorption. Notably, our proposed approach introduces a critical role for defect connectivity within the ZIM-based CPA, beyond the phase differences among different incident waves, further enhancing control capabilities. Our approach opens up promising avenues for advanced CPA control with versatile functionalities.

It is important to highlight that the underlying physics governing the CPA using 2D and 3D ZIM is fundamentally different. In 2D ZIM-based CPA [22, 23], the principle relies on the photonic doping effect [37–42], which however, is absent in 3D ZIM due to distinct electromagnetic wave behaviors [13, 33, 34]. The electromagnetic waves in 2D ZIM follow scalar wave equations, while they obey vector wave equations in 3D ZIM. Consequently, in 2D ZIM-based CPA, variations in geometrical and electromagnetic parameters (e.g., size, shape, and permittivity) significantly affect the absorption properties due to the photonic doping effect [22, 23]. Nevertheless, in 3D ZIM-based CPA, the absorption is primarily governed by the establishment of long-range connectivity among defects, rather than their details. As long as the long-range connectivity of defects is established, the CPA exhibits remarkable robustness against variations in the defects' geometrical and electromagnetic parameters.

In conclusion, we have highlighted the essential role of defect connectivity within 3D ZIM for realizing and controlling the CPA. The intriguing properties of 3D ZIM-based CPA have been elucidated, revealing its sensitivity to perturbations in defect connectivity, while demonstrating remarkable robustness against deformations of defects, changes in size and shape of the ZIM, and variations in number and orientation of incident channels, as long as the long-range connectivity is maintained. Furthermore, geometry-invariant multichannel CPA based on 3D ZIM, as well as the practical implementation using PhCs exhibiting a Dirac-like cone dispersion have been demonstrated. These findings open up exciting possibilities for advanced and flexible control of absorption with potential applications in various fields, such as sensors, modulators, and switches.

Research funding: Natural Science Foundation of Jiangsu Province (Grant No. BK20221354), the National Natural Science Foundation of China (Grant No. 12274315), the National Key R&D Program of China (Grant No. 2022YFA1404400), Undergraduate Training Program for Innovation and Entrepreneurship, Soochow University, and a Project Funded by the Priority Academic Program Development of Jiangsu Higher Education Institutions (PAPD).
Author contributions: All authors have accepted responsibility for the entire content of this manuscript and approved its submission.
Conflict of interest: Authors state no conflicts of interest.
Data availability: Data underlying the results presented in this paper are not publicly available at this time but may be obtained from the authors upon reasonable request.

References

[1] C. M. Watts, X. Liu, and W. J. Padilla, "Metamaterial electromagnetic wave absorbers," *Adv. Mater.*, vol. 24, pp. OP98—OP120, 2012.
[2] Y. Cui, Y. He, Y. Jin, et al., "Plasmonic and metamaterial structures as electromagnetic absorbers," *Laser Photon. Rev.*, vol. 8, pp. 495—520, 2014.
[3] Y. Ra'Di, C. R. Simovski, and S. A. Tretyakov, "Thin perfect absorbers for electromagnetic waves: theory, design, and realizations," *Phys. Rev. Appl.*, vol. 3, p. 037001, 2015.
[4] Y. D. Chong, L. Ge, H. Cao, and A. D. Stone, "Coherent perfect absorbers: time-reversed lasers," *Phys. Rev. Lett.*, vol. 105, p. 053901, 2010.
[5] W. Wan, Y. Chong, L. Ge, H. Noh, A. D. Stone, and H. Cao, "Time-reversed lasing and interferometric control of absorption," *Science*, vol. 331, pp. 889—892, 2011.
[6] D. G. Baranov, A. Krasnok, T. Shegai, A. Alù, and Y. Chong, "Coherent perfect absorbers: linear control of light with light," *Nat. Rev. Mater.*, vol. 2, p. 17064, 2017.
[7] Y. Slobodkin, G. Weinberg, H. Hörner, K. Pichler, S. Rotter, and O. Katz, "Massively degenerate coherent perfect absorber for arbitrary wavefronts," *Science*, vol. 377, pp. 995—998, 2022.
[8] S. Longhi, "PT-symmetric laser absorber," *Phys. Rev. A*, vol. 82, p. 031801(R), 2010.
[9] Y. D. Chong, L. Ge, and A. D. Stone, "PT-symmetry breaking and laser-absorber modes in optical scattering systems," *Phys. Rev. Lett.*, vol. 106, p. 093902, 2011.
[10] Y. Sun, W. Tan, H. Li, J. Li, and H. Chen, "Experimental demonstration of a coherent perfect absorber with PT phase transition," *Phys. Rev. Lett.*, vol. 112, p. 143903, 2014.
[11] Z. J. Wong, Y. Xu, J. Kim, et al., "Lasing and anti-lasing in a single cavity," *Nat. Photonics*, vol. 10, pp. 796—801, 2016.
[12] P. Bai, K. Ding, G. Wang, et al., "Simultaneous realization of a coherent perfect absorber and laser by zero-index media with both gain and loss," *Phys. Rev. A*, vol. 94, p. 063841, 2016.

[13] J. Luo, J. Li, and Y. Lai, "Electromagnetic impurity-immunity induced by parity-time symmetry," *Phys. Rev. X*, vol. 8, p. 031035, 2018.
[14] J. Y. Lee and P. Chen, "Wave propagation, bi-directional reflectionless, and coherent perfect absorption-lasing in finite periodic PT-symmetric photonic systems," *Nanophotonics*, vol. 12, pp. 3099—3108, 2023.
[15] M. B. Pu, Q. Feng, M. Wang, et al., "Ultrathin broadband nearly perfect absorber with symmetrical coherent illumination," *Opt. Express*, vol. 20, pp. 2246—2254, 2012.
[16] S. Li, J. Luo, S. Anwar, et al., "Broadband perfect absorption of ultrathin conductive films with coherent illumination: superabsorption of microwave radiation," *Phys. Rev. B*, vol. 91, p. 220301(R), 2015.
[17] J. Zhang, X. Wei, M. Premaratne, and W. Zhu, "Experimental demonstration of an electrically tunable broadband coherent perfect absorber based on a graphene-electrolyte-graphene sandwich structure," *Photon. Res.*, vol. 7, p. 868, 2019.
[18] L. Wang, J. Hu, J. Du, and K. Di, "Broadband coherent perfect absorption by cavity coupled to three-level atoms in linear and nonlinear regimes," *New J. Phys.*, vol. 23, p. 123040, 2021.
[19] C. Wang, X. Shen, H. Chu, et al., "Realization of broadband coherent perfect absorption of spoof surface plasmon polaritons," *Appl. Phys. Lett.*, vol. 120, p. 171703, 2022.
[20] P. Luo, G. Lan, J. Nong, X. Zhang, T. Xu, and W. Wei, "Broadband coherent perfect absorption employing an inverse-designed metasurface via genetic algorithm," *Opt. Express*, vol. 30, p. 34429, 2022.
[21] Z. Zhang, Q. Xie, L. Guo, et al., "Dual-controlled tunable dual-band and ultra-broadband coherent perfect absorber in the THz range," *Opt. Express*, vol. 30, p. 30832, 2022.
[22] J. Luo, B. Liu, Z. H. Hang, and Y. Lai, "Coherent perfect absorption via photonic doping of zero-index media," *Laser Photon. Rev.*, vol. 2018, p. 1800001, 2018.
[23] D. Wang, J. Luo, Z. Sun, and Y. Lai, "Transforming zero-index media into geometry-invariant coherent perfect absorbers via embedded conductive films," *Opt. Express*, vol. 29, p. 5247, 2021.
[24] C. T. Chan, Z. H. Hang, and X. Huang, "Dirac dispersion in two-dimensional photonic crystals," *Adv. Optoelectron.*, vol. 2012, pp. 1—11, 2012.
[25] I. Liberal and N. Engheta, "Near-zero refractive index photonics," *Nat. Photonics*, vol. 11, pp. 149—158, 2017.
[26] X. Niu, X. Hu, S. Chu, and Q. Gong, "Epsilon-near-zero photonics: a new platform for integrated devices," *Adv. Opt. Mater.*, vol. 2018, p. 1701292, 2018.
[27] D. I. Vulis, O. Reshef, P. Camayd-Muñoz, and E. Mazur, "Manipulating the flow of light using Dirac-cone zero-index metamaterials," *Rep. Prog. Phys.*, vol. 82, p. 012001, 2019.
[28] Z. Guo, H. Jiang, and H. Chen, "Zero-index and hyperbolic metacavities: fundamentals and applications," *J. Phys. D*, vol. 55, p. 083001, 2021.
[29] Y. Li, C. T. Chan, and E. Mazur, "Dirac-like cone-based electromagnetic zero-index metamaterials," *Light Sci. Appl.*, vol. 10, p. 203, 2021.
[30] J. Wu, Z. T. Xie, Y. Sha, H. Y. Fu, and Q. Li, "Epsilon-near-zero photonics: infinite potentials," *Photon. Res.*, vol. 9, p. 1616, 2021.
[31] J. Luo and Y. Lai, "Hermitian and non-Hermitian Dirac-like cones in photonic and phononic structures," *Front. Phys.*, vol. 10, p. 845624, 2022.
[32] X. Qin, W. Sun, Z. Zhou, P. Fu, H. Li, and Y. Li, "Waveguide effective plasmonics with structure dispersion," *Nanophotonics*, vol. 11, pp. 1659—1676, 2022.
[33] J. Luo, Z. H. Hang, C. T. Chan, and Y. Lai, "Unusual percolation threshold of electromagnetic waves in double-zero medium embedded with random inclusions," *Laser Photon. Rev.*, vol. 9, pp. 523—529, 2015.
[34] C. Xu, H. Chu, J. Luo, Z. H. Hang, Y. Wu, and Y. Lai, "Three-dimensional electromagnetic void space," *Phys. Rev. Lett.*, vol. 127, p. 123902, 2021.
[35] C. Wang, R. Shi, L. Gao, A. S. Shalin, and J. Luo, "Quenching of second-harmonic generation by epsilon-near-zero media," *Photon. Res.*, vol. 11, pp. 1437—1448, 2023.
[36] A. S. Shalin, P. Ginzburg, A. A. Orlov, et al., "Scattering suppression from arbitrary objects in spatially dispersive layered metamaterials," *Phys. Rev. B*, vol. 91, p. 125426, 2015.
[37] I. Liberal, A. M. Mahmoud, Y. Li, B. Edwards, and N. Engheta, "Photonic doping of epsilon-near-zero media," *Science*, vol. 355, pp. 1058—1062, 2017.
[38] I. Liberal, Y. Li, and N. Engheta, "Reconfigurable epsilon-near-zero metasurfaces via photonic doping," *Nanophotonics*, vol. 7, pp. 1117—1127, 2018.
[39] M. Coppolaro, M. Moccia, G. Castaldi, N. Engheta, and V. Galdi, "Non-Hermitian doping of epsilon-near-zero media," *Proc. Natl. Acad. Sci. USA*, vol. 117, pp. 13921—13928, 2020.
[40] Z. Zhou, H. Li, W. Sun, et al., "Dispersion coding of ENZ media via multiple photonic dopants," *Light Sci. Appl.*, vol. 11, p. 207, 2022.
[41] H. Li, Z. Zhou, Y. He, et al., "Geometry-independent antenna based on epsilon-near-zero medium," *Nat. Commun.*, vol. 13, p. 3568, 2022.
[42] H. Li, P. Fu, Z. Zhou, et al., "Performing calculus with epsilon-near-zero metamaterials," *Sci. Adv.*, vol. 8, p. eabq6198, 2022.
[43] F. R. Yang, K. P. Ma, Y. X. Qian, and T. Itoh, "A novel TEM waveguide using uniplanar compact photonic-bandgap (UC-PBG) structure," *IEEE Trans. Microw. Theory Tech.*, vol. 47, pp. 2092—2098, 1999.
[44] J. Luo, S. Li, B. Hou, and Y. Lai, "Unified theory for perfect absorption in ultrathin absorptive films with constant tangential electric or magnetic fields," *Phys. Rev. B*, vol. 90, p. 165128, 2014.
[45] S. M. Rao, J. J. F. Heitz, T. Roger, N. Westerberg, and D. Faccio, "Coherent control of light interaction with graphene," *Opt. Lett.*, vol. 39, p. 5345, 2014.
[46] C. T. Chan, X. Huang, F. Liu, and Z. H. Hang, "Dirac dispersion and zero-index in two dimensional and three dimensional photonic and phononic systems," *Prog. Electromagn. Res. B*, vol. 44, pp. 164—190, 2012.
[47] M. Song, P. Belov, and P. Kapitanova, "Wireless power transfer based on dielectric resonators with colossal permittivity," *Appl. Phys. Lett.*, vol. 109, p. 223902, 2016.
[48] X. Huang, Y. Lai, Z. H. Hang, H. Zheng, and C. T. Chan, "Dirac cones induced by accidental degeneracy in photonic crystals and

zero-refractive-index materials," *Nat. Mater.*, vol. 10, pp. 582—586, 2011.

[49] P. Moitra, Y. Yang, Z. Anderson, I. I. Kravchenko, D. P. Briggs, and J. Valentine, "Realization of an all-dielectric zero-index optical metamaterial," *Nat. Photonics*, vol. 7, pp. 791—795, 2013.

[50] Y. Li, S. Kita, P. Muñoz, et al., "On-chip zero-index metamaterials," *Nat. Photonics*, vol. 9, pp. 738—742, 2015.

[51] J. Luo, Y. Yang, Z. Yao, et al., "Ultratransparent media and transformation optics with shifted spatial dispersions," *Phys. Rev. Lett.*, vol. 117, p. 223901, 2016.

Supplementary Material: This article contains supplementary material (https://doi.org/10.1515/nanoph-2023-0485).